A Virgo Environmental Survey Tracing Ionised Gas Emission (VESTIGE)

A. Boselli, M. Fossati, A. Longobardi, G. Consolandi, P. Amram, M. Sun, P. Andreani, M. Boquien, J. Braine, F. Combes, et al.

▶ **To cite this version:**

A. Boselli, M. Fossati, A. Longobardi, G. Consolandi, P. Amram, et al.. A Virgo Environmental Survey Tracing Ionised Gas Emission (VESTIGE): V. Properties of the ionised gas filament of M 87. Astronomy and Astrophysics - A&A, 2019, 623, pp.A52. 10.1051/0004-6361/201834492 . hal-01903254

HAL Id: hal-01903254
https://hal.science/hal-01903254

Submitted on 24 Nov 2020

HAL is a multi-disciplinary open access archive for the deposit and dissemination of scientific research documents, whether they are published or not. The documents may come from teaching and research institutions in France or abroad, or from public or private research centers.

L'archive ouverte pluridisciplinaire **HAL**, est destinée au dépôt et à la diffusion de documents scientifiques de niveau recherche, publiés ou non, émanant des établissements d'enseignement et de recherche français ou étrangers, des laboratoires publics ou privés.

A&A 623, A52 (2019)
https://doi.org/10.1051/0004-6361/201834492
© A. Boselli et al. 2019

Astronomy & Astrophysics

A Virgo Environmental Survey Tracing Ionised Gas Emission (VESTIGE)

V. Properties of the ionised gas filament of M 87⋆

A. Boselli[1], M. Fossati[2,3], A. Longobardi[4], G. Consolandi[5], P. Amram[1], M. Sun[6], P. Andreani[7], M. Boquien[8], J. Braine[9], F. Combes[10,11], P. Côté[12], J. C. Cuillandre[13], P. A. Duc[14], E. Emsellem[7], L. Ferrarese[12], G. Gavazzi[15], S. Gwyn[11], G. Hensler[16], E. W. Peng[17,4], H. Plana[18], J. Roediger[12], R. Sanchez-Janssen[19], M. Sarzi[20], P. Serra[21], and G. Trinchieri[5]

[1] Aix-Marseille Univ., CNRS, CNES, LAM, Marseille, France
e-mail: alessandro.boselli@lam.fr
[2] Max-Planck-Institut für Extraterrestrische Physik, Giessenbachstrasse, 85748 Garching, Germany
[3] Institute for Computational Cosmology and Centre for Extragalactic Astronomy, Department of Physics, Durham University, South Road, Durham DH1 3LE, UK
e-mail: matteo.fossati@durham.ac.uk
[4] Kavli Institute for Astronomy and Astrophysics, Peking University, Beijing 100871, PR China
e-mail: alongobardi@pku.edu.cn
[5] INAF – Osservatorio Astronomico di Brera, via Brera 28, 20159 Milano, Italy
[6] Department of Physics and Astronomy, University of Alabama in Huntsville, Huntsville, AL 35899, USA
[7] European Southern Observatory, Karl-Schwarzschild-Strasse 2, 85748 Garching, Germany
[8] Centro de Astronomá (CITEVA), Universidad de Antofagasta, Avenida Angamos 601, Antofagasta, Chile
[9] Laboratoire d'Astrophysique de Bordeaux, Univ. Bordeaux, CNRS, B18N, allée Geoffroy Saint-Hilaire, 33615 Pessac, France
[10] Collège de France, 11 Pl. M. Berthelot, 75005 Paris, France
[11] LERMA, Observatoire de Paris, CNRS, PSL Research University, Sorbonne Universités, UPMC Univ. Paris 06, 75014 Paris, France
[12] NRC Herzberg Astronomy and Astrophysics, 5071 West Saanich Road, Victoria, BC V9E 2E7, Canada
[13] AIM, CEA, CNRS, Université Paris-Saclay, Université Paris Diderot, Sorbonne Paris Cité, Observatoire de Paris, PSL University, 91191 Gif-sur-Yvette Cedex, France
[14] Observatoire Astronomique de Strasbourg, UMR 7750, 11 rue de l'Université, 67000 Strasbourg, France
[15] Universitá di Milano-Bicocca, Piazza della Scienza 3, 20100 Milano, Italy
[16] Department of Astrophysics, University of Vienna, Türkenschanzstrasse 17, 1180 Vienna, Austria
[17] Department of Astronomy, Peking University, Beijing 100871, PR China
[18] Laboratório de Astrofísica Teórica e Observacional, Universidade Estadual de Santa Cruz, 45650-000 Ilhéus, BA, Brazil
[19] UK Astronomy Technology Centre, Royal Observatory Edinburgh, Blackford Hill, Edinburgh EH9 3HJ, UK
[20] Centre for Astrophysics Research, University of Hertfordshire, Hatfield AL10 9AB, UK
[21] Osservatorio Astronomico di Cagliari, Via della Scienza 5, 09047 Selargius, Cagliari, Italy

Received 23 October 2018 / Accepted 4 December 2018

ABSTRACT

We observed the giant elliptical galaxy M 87 during the Virgo Environmental Survey Tracing Galaxy Evolution (VESTIGE), a blind narrow-band Hα+[NII] imaging survey of the Virgo cluster carried out with MegaCam at the Canada French Hawaii Telescope (CFHT). The deep narrow-band image confirmed the presence of a filament of ionised gas extending up to $\simeq$3 kpc in the north-western direction and $\simeq$8 kpc to the southeast, with a couple of plumes of ionised gas, the weakest of which, at $\simeq$18 kpc from the nucleus, was previously unknown. The analysis of deep optical images taken from the NGVS survey confirms that this gas filament is associated with dust seen in absorption which is now detected up to $\simeq$2.4 kpc from the nucleus. We also analysed the physical and kinematical properties of the ionised gas filament using deep IFU MUSE data covering the central 4.8×4.8 kpc^2 of the galaxy. The spectroscopic data confirm a perturbed kinematics of the ionised gas, with differences in velocity of $\simeq$700–800 km s^{-1} on scales of $\lesssim$1 kpc. The analysis of 2D diagnostic diagrams and the observed relationship between the shock-sensitive [OI]/Hα line ratio and the velocity dispersion of the gas suggest that the gas is shock-ionised.

Key words. galaxies: clusters: general – galaxies: clusters: individual: Virgo – galaxies: evolution – galaxies: interactions – galaxies: ISM – galaxies: individual: M 87

⋆ Based on observations obtained with MegaPrime/MegaCam, a joint project of CFHT and CEA/DAPNIA, at the Canada-France-Hawaii Telescope (CFHT) which is operated by the National Research Council (NRC) of Canada, the Institut National des Sciences de l'Univers of the Centre National de la Recherche Scientifique (CNRS) of France and the University of Hawaii. Based on observations made with ESO Telescopes at the La Silla Paranal Observatory under programme ID 60.A-9312.

Open Access article, published by EDP Sciences, under the terms of the Creative Commons Attribution License (http://creativecommons.org/licenses/by/4.0), which permits unrestricted use, distribution, and reproduction in any medium, provided the original work is properly cited.

1. Introduction

Giant ellipticals in the centre of rich clusters are among the most massive and luminous objects in the local universe. They share with the cluster several properties such as a diffuse X-ray and stellar emission and a similar rest-frame velocity (e.g. Sarazin 1986). They are often used to trace the properties of the cluster dark matter halo in the study of the galaxy-halo connection (galaxy conformity), making them unique systems among all galaxy populations. Located deep in the potential well of a large dynamic structure, they have been formed through the accretion of baryonic matter in its different forms, from the diffuse intracluster medium (ICM) through cooling flows (Cowie & Binney 1977; Fabian & Nulsen 1977; Fabian 1994), to the cannibalism of other galaxies orbiting within the cluster (Ostriker & Tremaine 1975). White (1976), Malumuth & Richstone (1984), Merritt (1985), Byrd & Valtonen (1990), and through multiple merging events that occurred during the formation of the cluster itself (e.g. De Lucia & Blaizot 2007; Boselli et al. 2014).

Among these objects, the elliptical galaxy M 87 (NGC 4486, 3C274, Virgo A) in the centre of Virgo is by far the most studied massive galaxy in the centre of a cluster, but also one of the most studied galaxies ever. At a distance of only 16.5 Mpc (Mei et al. 2007), M 87 can be fully resolved at almost all frequencies, from the X-rays to the radio centimetric. At this distance, one arcsec corresponds to ≃80 pc, a small size compared to the optical extension of the galaxy which has an isophotal radius of ≃25 kpc (Cortese et al. 2012). This galaxy is a powerful radio source (Baade & Minkowski 1954) characterised by a prominent jet and two extended radio lobes (e.g. Hines et al. 1989; Owen et al. 2000). It also has a characteristic X-ray emission showing long filaments of hot gas extending up to 22 kpc to the east and 28 kpc to the south embedded in a diffuse halo (e.g. Young et al. 2002; Forman et al. 2007; Churazov et al. 2008; Werner et al. 2010).

Similar filamentary structures have also been observed in narrow-band Hα imaging (Arp 1967; Ford & Butcher 1979; Baum et al. 1988; Heckman et al. 1989; Sparks et al. 1993, 2004; Gavazzi et al. 2000; Werner et al. 2010), in different UV lines with HST (Sparks et al. 2009, Anderson & Sunayaev 2018), and in the [CII]λ158 μm line with *Herschel* (Werner et al. 2013), indicating the multi-temperature nature of the gas. In particular, the narrow-band Hα imaging data revealed a very complex filament extending to the southeast up to ≃8 kpc from the nucleus, with a few patchy regions, whose nature and origin are still not fully understood.

The Hα emission line traces the distribution of the ionised hydrogen with a typical temperature of ≃10^4 K (Osterbrock & Ferland 2006). For this reason this line has often been used to look for cooling flows in the centre of rich clusters of galaxies (e.g. Conselice et al. 2001). In spiral galaxies, where the gas is ionised by the young stellar populations, the Hα line is an excellent tracer of the recent star formation activity (Kennicutt 1998; Boselli et al. 2009). In early-type galaxies the gas can be ionised by a residual star formation activity (Kaviraj et al. 2007; Gavazzi et al. 2018) or by a low level ionisation due to hot, evolved (post-asymptotic giant branch) stars (Gomes et al. 2016; Belfiore et al. 2016), the same stellar population responsible for the UV upturn observed in the far ultraviolet (FUV; O'Connell 1999; Boselli et al. 2005). In M 87 the gas can also be shock-excited by the central AGN or by the radio jet and counter-jet in the expanding lobes (Dopita & Sutherland 1995; Dopita et al. 1997), or heated by thermal conduction (Sparks et al. 2004; McDonald et al. 2010). The gas filament could be hot gas accreted from the intracluster medium cooling to $T \simeq 10^4$ K, or cold gas stripped from a gas-rich cluster galaxy after a gravitational interaction or lost during a recent ram pressure stripping event while crossing the halo of M 87 (Sparks et al. 1993; Weil et al. 1997; Mayer et al.2006).

We recently observed M 87 as part of VESTIGE (A Virgo Environmental Survey Tracing Ionised Gas Emission), a CFHT large programme designed to make a blind, deep narrow-band Hα imaging survey of the whole Virgo cluster up to its virial radius (104 deg^2, Boselli et al. 2018a). The core of the cluster, including M 87 and its surrounding regions, was mapped during the 2017A observing campaign. Thanks to a tuned observing strategy and a specific data-reduction technique optimised to detect extended, low-surface-brightness features in the continuum-subtracted narrow-band images, the VESTIGE data surpass those available in the literature in terms of sensitivity and angular resolution, passing from a limiting surface brightness of Σ(Hα + [NII]) $\simeq$ 10^{-16} erg s^{-1} cm^{-2} arcsec^{-2} to Σ(Hα + [NII]) $\simeq$ 5×10^{-18} erg s^{-1} cm^{-2} arcsec^{-2}. The success of this original observing and data reduction strategy was demonstrated by the detection of extended tails of ionised gas in several Virgo spirals (Boselli et al. 2016, 2018a,b; Fossati et al. 2018). In this paper we present these new narrow-band imaging data obtained during the VESTIGE survey. We also present new photometric and spectroscopic data obtained at other frequencies useful for the study of the ionised gas filament. These include a deep spectroscopic IFU MUSE field in the central $1' \times 1'$ of the galaxy taken as part of the first instrument verification run (Emsellem et al. 2014), GALEX UV from the GUViCS survey (Boselli et al. 2011), and optical images from the NGVS survey (Ferrarese et al. 2012). We then compare this new dataset with data at other frequencies available in the literature to have a complete view of the different phases of the interstellar medium (ISM) along the filament and in the surrounding ICM. Since the properties of the multi-temperature gas of M 87 have already been studied in detail in the past, we refer the reader to these publications (Sparks et al. 1993, 2004; Churazov et al. 2001, 2008; Young et al. 2002; Forman et al. 2007, 2017; Werner et al. 2013; Simionescu et al. 2018). Here we limit our analysis to the novelties brought by our new dataset. The paper is structured as follows: the VESTIGE and MUSE observations and data reduction are presented in Sect. 2, along with the multifrequency data available in the literature. In Sect. 3 we analyse the new dataset through a comparative multifrequency analysis. A discussion and conclusions are given in Sects. 4 and 5. Consistently with the other VESTIGE publications, we assume a distance of 16.5 Mpc for M 87 and the Virgo cluster (Gavazzi et al. 1999; Mei et al. 2007).

2. Observations and data reduction

2.1. Narrow-band imaging

M 87 and its surrounding regions were mapped during the first observing semester of the VESTIGE project (2017A; Boselli et al. 2018a for details). The observations were taken using MegaCam at the CFHT through the narrow-band filter MP9603 (λ_c = 6591 Å; $\Delta\lambda$ = 106 Å), which includes at the redshift of M 87 (vel = 1292 km s^{-1}, GOLDMine) the Hα line (λ = 6563 Å) and the two [NII] lines (λ = 6548, 6583 Å), and through the *r*-band filter for the stellar continuum subtraction. MegaCam is composed of 40 2048 × 4096 pixels CCDs with a pixel size of 0.187″ on the sky. The galaxy has been covered with 12 independent frames with a large dithering selected for the whole VESTIGE blind survey (15 arcmin in RA, 20 arcmin in Dec).

Each single exposure was of 600 s in the narrow-band Hα filter and 60 s in the broad-band r filter. The observations were carried out in good seeing conditions, with a typical seeing of 0.90 and 0.83 arcsec in the narrow-band and broad-band stacked frames, respectively.

The data were reduced following the VESTIGE standard procedures presented in Boselli et al. (2018a) and Fossati et al. (in prep.). This consists in using Elixir-LSB (Ferrarese et al. 2012), a data-reduction pipeline expressly designed to detect extended low-surface-brightness features associated with perturbed galaxies through an accurate determination and subtraction of any extended feature in the sky background.

The photometric calibration of the r-band frames was derived following the standard MegaCam calibration procedures (Gwyn 2008), as extensively described in Boselli et al. (2018a). The calibration in the narrow-band filter was done as described in Fossati et al. (in prep.). The typical uncertainty of VESTIGE in both bands is of $\lesssim$0.02–0.03 mag.

The subtraction of the stellar continuum for the determination of the image of the emitting gas is critical in early-type galaxies such as M 87 which are characterised by a strong stellar emission in their centre, where the ionised gas is expected to be detected.

Given the wide band of the r filter (λ_c = 6404 Å; $\Delta\lambda$ = 1480 Å) and the slight difference in the peak transmissivity of the two bands, the derivation of the stellar continuum in the narrow-band from the r-band depends on the spectral properties of the emitting source (Spector et al. 2012), and therefore also on the colour that in early-type galaxies is known to change radially from the core to the periphery (Boroson et al. 1983; Franx & Illingworth 1990; Suh et al. 2010; Roediger et al. 2011). As extensively described in Fossati et al. (in prep.), we used several hundred thousand unsaturated stars detected in the Hα narrow-band and in the r- and g-bands in the science frames to calibrate an empirical relation between the colour of the stars (expressed in AB magnitudes) and the normalisation factor:

$$\frac{r}{\mathrm{H}\alpha + [\mathrm{NII}]} = r - 0.1713 \times (g - r) + 0.0717. \quad (1)$$

We applied this normalisation pixel by pixel on the stacked frame before the subtraction of the stellar continuum. The $g - r$ colour map of the galaxy was derived using the g-band frame taken with MegaCam during the NGVS survey (Ferrarese et al. 2012). To avoid the introduction of any extra noise in the sky regions, where there is no stellar continuum, this colour-dependent normalisation is applied only whenever the signal in the r- and g-bands has a signal-to-noise ratio (S/N) greater than 1. The continuum-subtracted image is then multiplied by the filter width (106 Å) to obtain the values of the line flux per pixel. The resulting Hα+[NII] stellar-continuum-subtracted image of M 87 is shown in Fig. 1. The quality of this image is excellent: indeed, there are no extended dark regions often observed whenever the stellar continuum is over subtracted.

The total observed flux of the galaxy (corrected for Galactic attenuation using the Schlegel et al. (1998) dust map recalibrated with Schlafly & Finkbeiner (2011) and assuming the Fitzpatrick (1999) Galactic attenuation curve) is log f(Hα + [NII]) = -11.66 ± 0.04 erg s^{-1} cm^{-2} and the equivalent width Hα+[NII]E.W. = 2.1 ± 0.2 Å and is dominated by the emission of the filament.

2.2. MUSE spectroscopy

M 87 was observed in 2014 with MUSE during the first instrument science verification run at the VLT. Details of the observations and data reduction are given in Emsellem et al. (2014) and Sarzi et al. (2018). MUSE provides a spectroscopic data cube on a rectangular $1' \times 1'$ field with spaxels of $0.2'' \times 0.2''$. The spectra cover the 4800–9000 Å range, with an instrumental resolution of $\sim$60 km s^{-1} at 5500 Å. Two 1800 s exposures were taken on the centre of the galaxy. Each exposure was followed by a 900 s exposure in the outskirts of the galaxy for an accurate determination of the sky background. The data were reduced using the v1.6 MUSE standard pipeline, as described in Sarzi et al. (2018). To subtract the stellar continuum emission and remove any possible contamination due to the underlying stellar absorption on the main Balmer lines we fitted the spectra using pPXF and GANDALF (Cappellari & Emsellem 2004; Sarzi et al. 2006). This code simultaneously models the stellar continuum and the emission lines in individual spaxels. The stellar continuum is modelled with a superposition of stellar templates convolved by the stellar line-of-sight velocity distribution, while the gas emission and kinematics were derived assuming a Gaussian line profile. Stellar templates were constructed using the MILES library (Vazdekis et al. 2010). We then fit the emission line (Hβ λ4861, [OIII]λ4959,5007, [OI]λ6300,6364, [NII]λ6548,6583, Hα λ6563, [SII]λ6716,6731, [SIII]λ9069) using the KUBEVIZ code as in Fossati et al. (2016). Groups of lines were fitted simultaneously using a combination of 1D Gaussian functions with fixed relative velocities. The noise was measured from the "stat" data cube and renormalised on the line fluxes to take into account the correlated noise introduced by resampling and smoothing, as extensively described in Fossati et al. (2016). Figure 2 shows the Hα emission line map and its S/N map derived for a $S/N > 5$.

2.3. Ultraviolet

Ultraviolet data can be used to identify the nature of the ionising source of the gas filaments observed in Fig. 1. Several GALEX exposures, available in both the FUV (λ_c = 1539 Å) and NUV (λ_c = 2316 Å) bands, were collected during the GUViCS survey of the cluster (Boselli et al. 2011). We combined the available frames with a sufficient S/N and obtained deep UV images of M 87 with a typical integration time of 3278 s in the FUV and 16267 s in the NUV, and used them to create the FUV/NUV colour image. M 87 has a diffuse light distribution in the UV, witnessing the presence of an evolved stellar population. The only evident structure in the image is the nucleus and the jet, which is present in both the FUV and NUV bands. The UV colour image does not show any clumpy structure which can be associated with a young stellar population. It is thus likely that, as in other massive early-type galaxies, the UV emission of M 87 is dominated by evolved stellar populations (UV upturn; O'Connell 1999; Boselli et al. 2005, 2014).

2.4. Visible

Optical data are essential to see the distribution of dust seen in absorption. For M 87 this is critical since in this object dust outside the nuclear region has never been detected in emission even in the most recent *Spitzer* (Perlman et al. 2007; Bendo et al. 2012; Ciesla et al. 2014) and *Herschel* (Ciesla et al. 2012; Cortese et al. 2014) observations[1]. M 87 was observed with HST during the ACS Virgo Cluster Survey (VCS) in the F475W and

[1] The detection reported in these works is due to the synchrotron emission associated with the radio galaxy and its jet (Baes et al. 2010; Boselli et al. 2010).

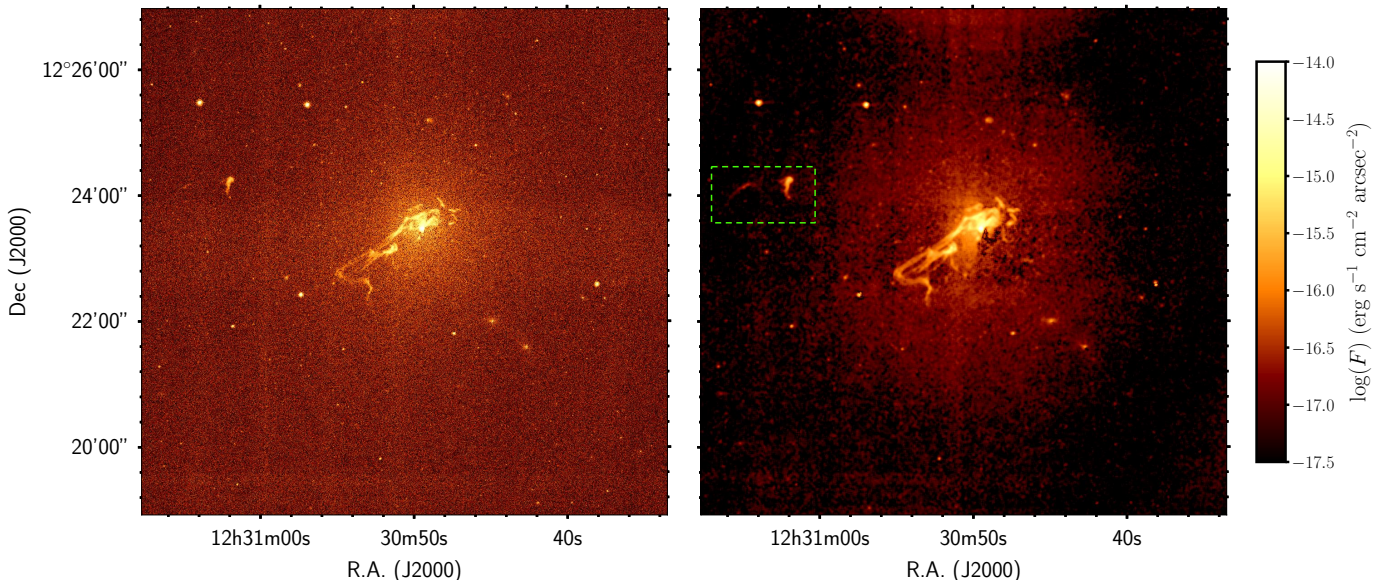

Fig. 1. *Left panel*: continuum-subtracted Hα+[NII] image of M 87 at full resolution. *Right panel*: continuum-subtracted Hα+[NII] image of M 87 after a 15×15 boxcar smoothing, corresponding to $\simeq$2.8 arcsec resolution. At the distance of M 87 (16.5 Mpc), 1 arcsec = 80 pc. The green dashed box indicates the zoomed-in region in Fig. 4. Smoothing reduces the noise in the outer parts, where the surface brightness sensitivity reaches $\Sigma(\mathrm{H}\alpha + [\mathrm{NII}]) \simeq 5 \times 10^{-18}$ erg s^{-1} cm^{-2} arcsec^{-2}.

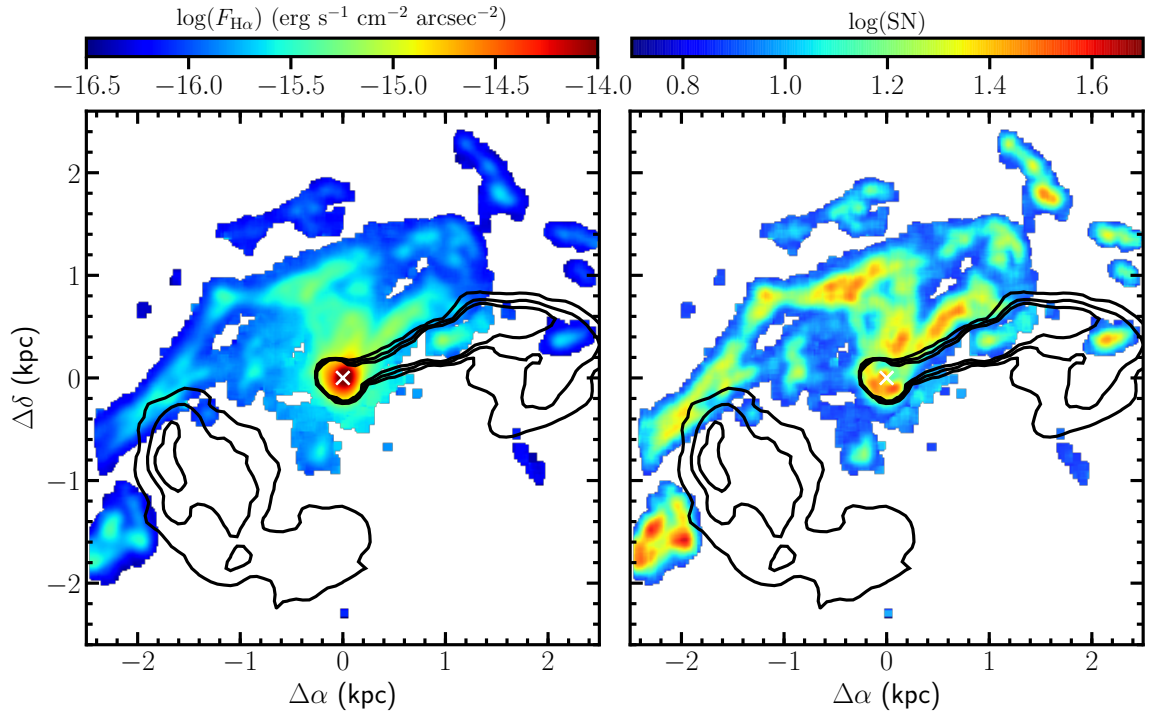

Fig. 2. The Hα emission line map (*left panel*) and its S/N (*right panel*) of the ionised gas derived from MUSE for a $S/N > 5$. The white cross in the centre of the frame indicates the position of the nucleus. The contour levels indicate the jet and counter-jet determined from 115 GHz ALMA data.

F850LP bands (~Sloan g and z; Côté et al. 2004) and in the F275W, F606W, and F814W bands by Bellini et al. (2015). The $g - z$ colour image of the central $\sim 1' \times 1'$ given in Ferrarese et al. (2006, their Fig. 1) and the galaxy-subtracted F275W, F606W, F814W colour image of Bellini et al. (2015, their Fig. 15) show a very faint filament of dust located in the western direction close to the position of the jet and patches of dust close to the centre.

The availability of deep and extended surveys targeting M 87, allows us to investigate whether dust is also present at larger distances from the centre of the galaxy. To do so we used the g-band imaging gathered by the NGVS, that in the galaxy central regions reaches optimal seeing conditions, 0.62″, and a depth of $g = 27.3$ mag or $\mu_g = 29.0$ mag arcsec^{-2}. The continuum emission from the galaxy was retrieved using the IRAF tasks ISOFIT and C-MODEL (Ciambur 2015) that allow for an accurate recovery of the galaxy surface-brightness profile, and therefore of a 2D model of the galaxy light. The resulting stellar-continuum-subtracted image of the inner $2' \times 2'$ is

shown in Fig. 3. Despite the poor image quality in the central 0.05′ × 0.05′, affected by the presence of the AGN (see Bellini et al. 2015 for the detection of dust in this region), Fig. 3 clearly shows the presence of dust in absorption. This is detected along the filament located to the north of the jet and in several other patchy features close to the centre as already identified by previous analyses (Sparks et al. 1993; Ferrarese et al. 2006; Bellini et al. 2015). However, the high-quality NGVS imaging also reveals a complicated network of dusty regions unknown so far. These are distributed around the galaxy in the western direction up to ∼2.4 kpc (0.5′).

At its highest densities the most prominent dust feature (red contours in Fig. 3) absorbs the continuum light with an extinction factor $A_g = 0.010 \pm 0.002 - 0.017 \pm 0.002$ mag. Such a value was estimated by comparing the NGVS g-band image with a dust-free model of the light distribution, the latter given by the ISOFIT 2D map of the galaxy light. We note that as consequence of the relatively small covering area of the dust the ISOFIT model is a good approximation of the unextinguished light. We also point out that this extinction factor perfectly agrees with the value obtained by Sparks et al. (1993). Here, assuming a standard gas-to-dust ratio $d \simeq 100$ and the relation

$$N(H) = 1.8 \times 10^{23} \frac{A_V}{d} [\mathrm{cm}^{-2}], \quad (2)$$

we can calculate the expected column density of the cold gas associated with the dust lane, $N(H) \simeq 1.8 \times 10^{19}$ cm^{-2}. This number is consistent with the upper limit in the column density derived from observations of HI in absorption (van Gorkom et al. 1989; Dwarakanath et al. 1994) or from other absorption line measurements and from the shape of the X-rays spectrum in the nucleus (Sabra et al. 2003). Given the size of the filament, we estimate as in Sparks et al. (1993) that the associated total mass of cold gas is $M_{\mathrm{gas,dust}} \simeq 2 \times 10^7\ M_\odot$.

3. Analysis

3.1. Narrow-band imaging

The continuum-subtracted narrow-band image of M 87 shows prominent ionised gas filaments extending from the nucleus along an axis with a position angle of ∼55 deg measured clockwise from the north. Most of the extended emission is on the south-eastern side of the galaxy, where the emitting gas is detected up to ∼8 kpc from the nucleus, while only ∼3 kpc in the northwestern direction. The typical surface density of the gas here is $\Sigma(\mathrm{H}\alpha + [\mathrm{NII}]) \simeq 2.5 \times 10^{-17}$ erg s^{-1} cm^{-2} arcsec^{-2} in the diffuse features while exceeding $\Sigma(\mathrm{H}\alpha + [\mathrm{NII}]) = 10^{-16}$ erg s^{-1} cm^{-2} arcsec^{-2} in the brightest clumpy regions. The total flux of the main central filament, measured within a rectangular box 133 × 35 arcsec inclined at 55 deg from the north (clockwise), is $f(\mathrm{H}\alpha + [\mathrm{NII}]) = 1.036 \times 10^{-12}$ erg s^{-1} cm^{-2}. Assuming that the typical [NII] contamination is $\log[\mathrm{NII}]_{6583}/\mathrm{H}\alpha \simeq 0.25$ as measured within the MUSE field (see Fig. 9), its total Hα luminosity is $L(\mathrm{H}\alpha) = 9.56 \times 10^{39}$ erg s^{-1}. As in Fossati et al. (2016) and Boselli et al. (2016) we can estimate the mean density and the total mass of the gas emitting in Hα along the filament using the relation:

$$L(\mathrm{H}\alpha) = n_\mathrm{e} n_\mathrm{p} \alpha^{\mathrm{eff}}_{\mathrm{H}\alpha} V f h \nu_{\mathrm{H}\alpha}, \quad (3)$$

(Osterbrock & Ferland 2006), where n_e and n_p are the number density of electrons and protons, $\alpha^{\mathrm{eff}}_{\mathrm{H}\alpha}$ is the Hα effective recombination coefficient ($\alpha^{\mathrm{eff}}_{\mathrm{H}\alpha} = 1.17 \times 10^{-13}$), V is the volume of the emitting region, f the volume filling factor, h the Planck's constant, and $\nu_{\mathrm{H}\alpha}$ the frequency of the Hα transition. Assuming a cylindrical distribution of the gas, with an orientation of 45 deg along the line of sight, and a filling factor $f = 0.1$, we estimate that the typical density of the gas is $n_\mathrm{e} \simeq 0.3$ cm^{-3} and its total mass $M(\mathrm{ionised})_{\mathrm{filament}} \simeq 6.9 \times 10^7\ M_\odot$. We stress, however, that this estimate, which is approximately a factor of ten larger than the mass derived by Sparks et al. (1993), is a very rough estimate given the very high uncertainty on the filling factor of the gas and on the volume of the filament.

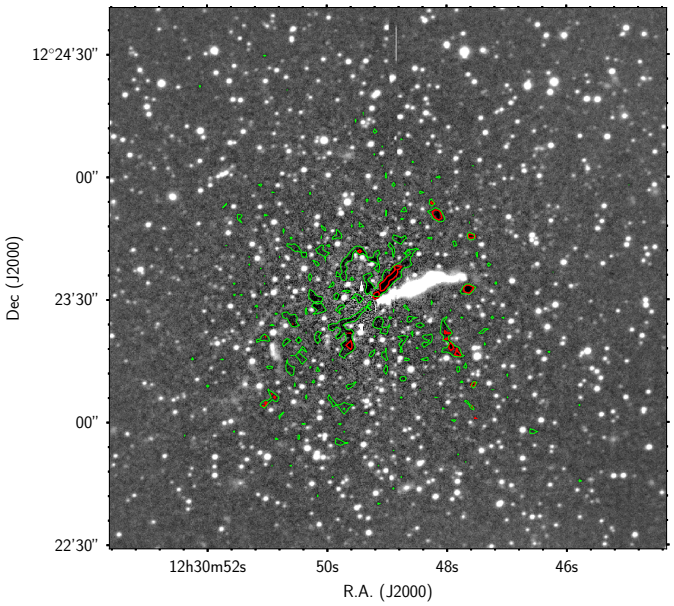

Fig. 3. Stellar continuum subtracted g-band image of M 87. The dark regions outlined by green contours are dusty structures detected in absorption. The red contour corresponds to $A_g = 0.010 \pm 0.002$. The bright elongated region is the jet and the point sources globular clusters and foreground stars.

The plume of ionised gas at ∼15 kpc to the east discovered by Gavazzi et al. (2000) is also evident given its high surface brightness ($\Sigma(\mathrm{H}\alpha + [\mathrm{NII}]) \simeq 10^{-16}$ erg s^{-1} cm^{-2} arcsec^{-2}, see Fig. 4). Figure 4 also shows a previously unknown banana-shaped, low-surface-brightness feature ($\Sigma(\mathrm{H}\alpha + [\mathrm{NII}]) = 5 \times 10^{-18}$ erg s^{-1} cm^{-2} arcsec^{-2}) ≃ 3 kpc long at ∼3 kpc east from this plume (18 kpc from the galaxy nucleus).

3.2. Spectroscopy

3.2.1. Gas kinematics

Figure 5 shows the velocity of the gas along the filament within the central 1′ × 1′ region. Thanks to the IFU mode of MUSE, the improvement in quality with respect to previous long-slit data is astonishing (Heckman et al. 1989; Sparks et al. 1993; Werner et al. 2013). Figure 6 shows the map of the velocity dispersion of the gas. The gas does not follow any ordered motion. As already noticed by Sparks et al. (1993), the difference in velocity within the inner gas filament is very high, reaching 700–800 km s^{-1} on scales $\lesssim$1 kpc. On the contrary, the velocity dispersion is ≃100 km s^{-1} and is fairly uniform over the gas filament, with the only exception being on the nucleus where it reaches ≃450 km s^{-1} due to the presence of an AGN. These velocity dispersions are generally larger than those measured within the tails of ionised gas observed in other perturbed cluster galaxies where these values are reached only within limited regions

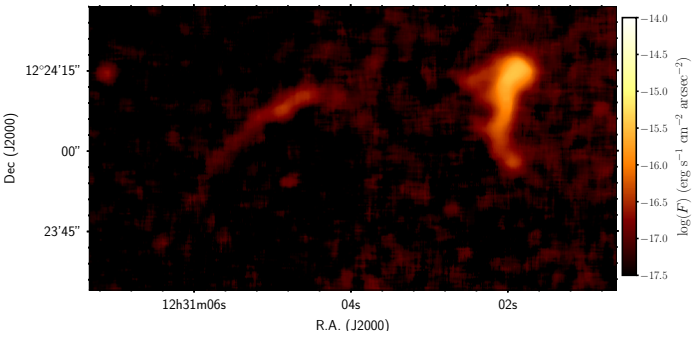

Fig. 4. Zoom on the plume of ionised gas discovered by Gavazzi et al. (2000; west), and on a new filament of ionised gas ≃3 kpc long (east). This zoomed region is indicated with a dashed green box in Fig. 1.

well outside the optical disc (Fumagalli et al. 2014; Consolandi et al. 2017; Poggianti et al. 2017; Bellhouse et al. 2017). For comparison, within the same MUSE field the velocity dispersion of the stellar component goes from ≃370 km s^{-1} in the central 2 arcsec (160 pc) to ≃260 km s^{-1} at ∼1.6 kpc, whereas the velocity rotation is always ≲10 km s^{-1} (Emsellem et al. 2014). The steep gradient in the velocity field observed in the regions at (−1.4; 0.0) kpc from the nucleus (Fig. 5, left panel), which is also characterised by a high velocity dispersion (Fig. 6, left panel) (and a high uncertainty on both the rotational velocity and the velocity dispersion, Figs. 5 and 6, right panels) suggests the presence of two physically and kinematically distinct components in the ionised gas. Cold gas has been detected in the bright ionised gas region at the southeast edge of the counter-jet radio lobe at (−2.2; −1.5) kpc from the nucleus through the emission of the ^{12}CO(2–1) (Simionescu et al. 2018) and [CII] (Werner et al. 2013) lines. Their recessional velocity is consistent within the errors.

Sparks et al. (1993), using geometrical arguments based on the presence of a dust lane absorbing the stellar emission, concluded that the associated gas filament in the western direction is in the foreground, and thus it is flowing out from the nucleus. Using similar arguments based on the relative position of the ionised gas filament and of the radio lobe, combined with the lack of any dust component, they also concluded that the southeastern gas filament is in the background of the galaxy.

3.2.2. Emission line properties

Several gas emission lines in the MUSE spectral range (4800–9000 Å) can be used to derive the physical properties of the gas through diagnostic diagrams. The Hα/Hβ Balmer decrement is generally used to derive the dust attenuation within the ionised gas.

The Balmer decrement within the MUSE field is shown in Fig. 7. The Hα/Hβ ratio is fairly constant along the filament, with values close to Hα/H$\beta \simeq$ 2.8–3.5. These values are close to those expected whenever the gas is photoionised by the emission of young and massive stars and the dust content is low ($E(B-V) \lesssim 0.08$). Similar values, however, are also expected whenever the gas is collisionally heated by cosmic rays accelerated by magnetohydrodynamic waves in the filament (Hα/H$\beta \simeq$ 3.7–4.4; Ferland et al. 2009). The comparison of Figs. 7 and 3 gives a consistent picture where dust attenuation is at the origin of the observed Balmer decrement.

The [SII]λ6716 Å/[SII]λ6731 Å, on the other hand, is tightly connected to the density of the gas (Osterbrock & Ferland 2006). Figure 8 shows that within the inner 1′×1′ region of M 87 mapped by MUSE the sulphur doublet ratio smoothly increases from [SII]λ6716 Å/[SII]λ6731 Å ≃ 0.9 ($n_e \simeq 6\times10^2$ cm^{-3} assuming a temperature of 10^4 K and using the recent calibration of Proxauf et al. 2014) close to the nucleus to [SII]λ6716 Å/[SII]λ6731 Å ≃ 1.35 ($n_e \simeq 80$ cm^{-3}) at the edges of the field[2]. These low densities are similar to those encountered in other tails of ionised gas in perturbed cluster galaxies (e.g. Poggianti et al. 2017). We notice that a large [SII]λ6716 Å/[SII]λ6731 Å ≥ 1.4 ratio has also been measured by Gavazzi et al. (2000) in the plume of ionised gas at ∼15 kpc to the east.

Unfortunately the high noise induced by the bright stellar continuum in these inner regions prevents the detection of the weak [NII] line at λ = 5755 Å. Therefore, we are not able to estimate the variation of the gas temperature along the filament using the [NII]λ6548 + [NII]λ6583 Å/[NII]λ5755 Å line ratio (Osterbrock & Ferland 2006). The detection of the [CIV] line at λ 1549 Å by Sparks et al. (2012) in the ionised gas, however, suggests that the gas might reach temperatures of $T = 10^5$ K. At this temperature, the iron lines [FeXIV] at λ 5303 Å and [FeX] at λ 6374 Å should also be present (Heckman et al. 1989). As explained above, however, the detection of these weak emission lines is hampered by the bright stellar continuum.

Figure 9 shows the map of different line ratios within the MUSE field, including the shock-sensitive [OI]λ6300 Å/Hα, [SII]λ6716,6731 Å/Hα and [NII]λ6548,6583 Å/Hα line ratios (Rich et al. 2011). Figure 9 shows high values for all the shock-sensitive tracers, both close to the AGN or along the filament, suggesting that within these regions the gas is mainly ionised by shocks. For comparison, lower values ([OI]λ6300 Å/Hα = 0.18; [SII]λ6716,6731 Å/Hα = 0.53) have been measured in the plume of ionised gas discovered by Gavazzi et al. (2000) at 15 kpc east from the galaxy nucleus.

Figure 10 shows three typical line diagnostic diagrams generally referred to as BPT diagrams (Baldwin et al. 1981). Thanks to the IFU mode of MUSE and to its excellent sensitivity, the difference with respect to published BPT diagrams, all based on long-slit spectroscopy (Heckman et al. 1989; Crawford et al. 1999), is stunning. The three BPT diagrams consistently indicate that the gas filament is not photoionised by massive young stars, in agreement with the lack of young stellar associations in the UV images of the galaxy. All the points are indeed located to the upper right of the typical curves delimiting the position of HII regions from AGN. The handful of dots in the photoionisation regime in the upper and lower panels of Fig. 10 are located along the jet, and therefore their line ratio estimates are highly uncertain.

To identify the possible ionising source of the gas within the filament we plot in Fig. 11 the relationship between the velocity dispersion of the gas σ and the three different shock-sensitive line ratios [NII]λ6584/Hα, [SII]λ6716,6731 Å/Hα, and [OI]λ6300 Å/Hα. Points are colour-coded according to their distance from the galaxy centre.

A strong relationship between the two variables has been interpreted in the literature as a further indication that the gas is excited by shocks (Rich et al. 2011, 2015; Ho et al. 2014). A significant correlation is seen only in the [OI]λ6300 Å/Hα line ratio, consistently with what was found in previous works (Ho et al. 2014). Here the velocity dispersion of the gas increases with the shock-sensitive [OI]λ6300 Å/Hα line ratio roughly in two different ways: there is a very tight and steep relation spanning the whole range in velocity dispersion (0 ≲ vel ≲ 500 km s^{-1}) where

[2] These densities scales as $(10^4/T)^{-1/2}$ if the temperature is $T \neq 10^4$ K, Osterbrock & Ferland (2006).

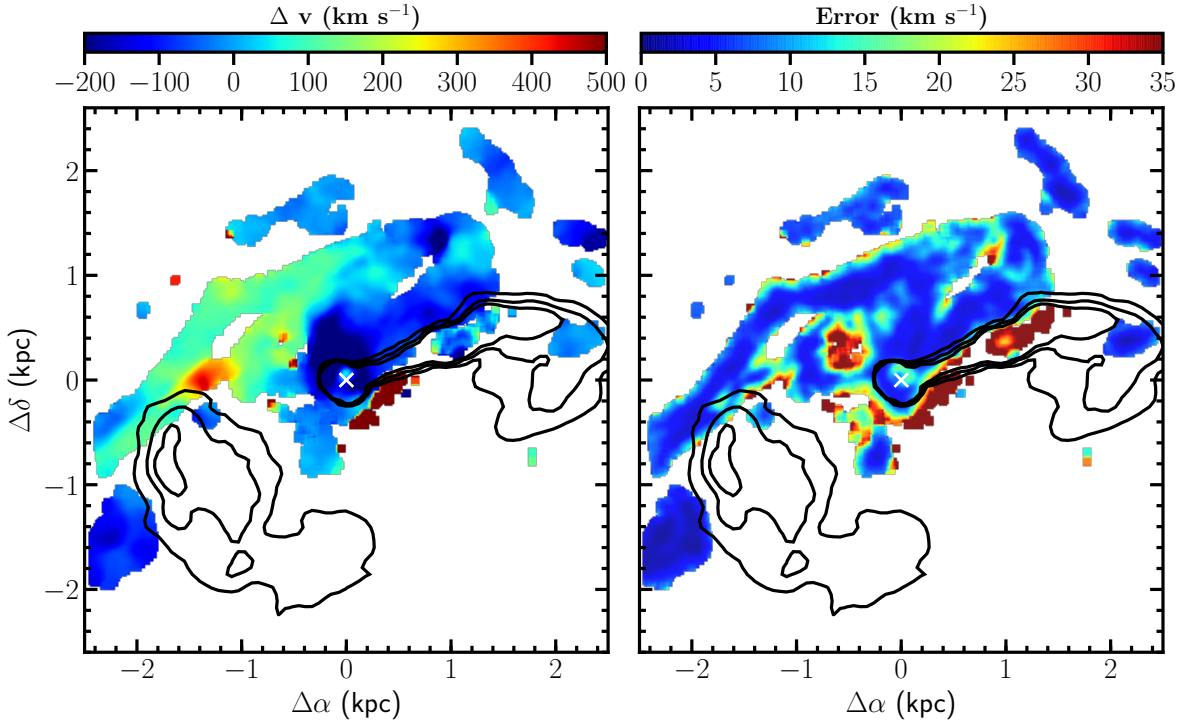

Fig. 5. Velocity map (*left panel*) and associated error (*right panel*) of the ionised gas derived from MUSE for emission lines with a $S/N > 10$. The velocity of the gas is given relative to the systemic velocity of the galaxy of 1292 km s^{-1}.

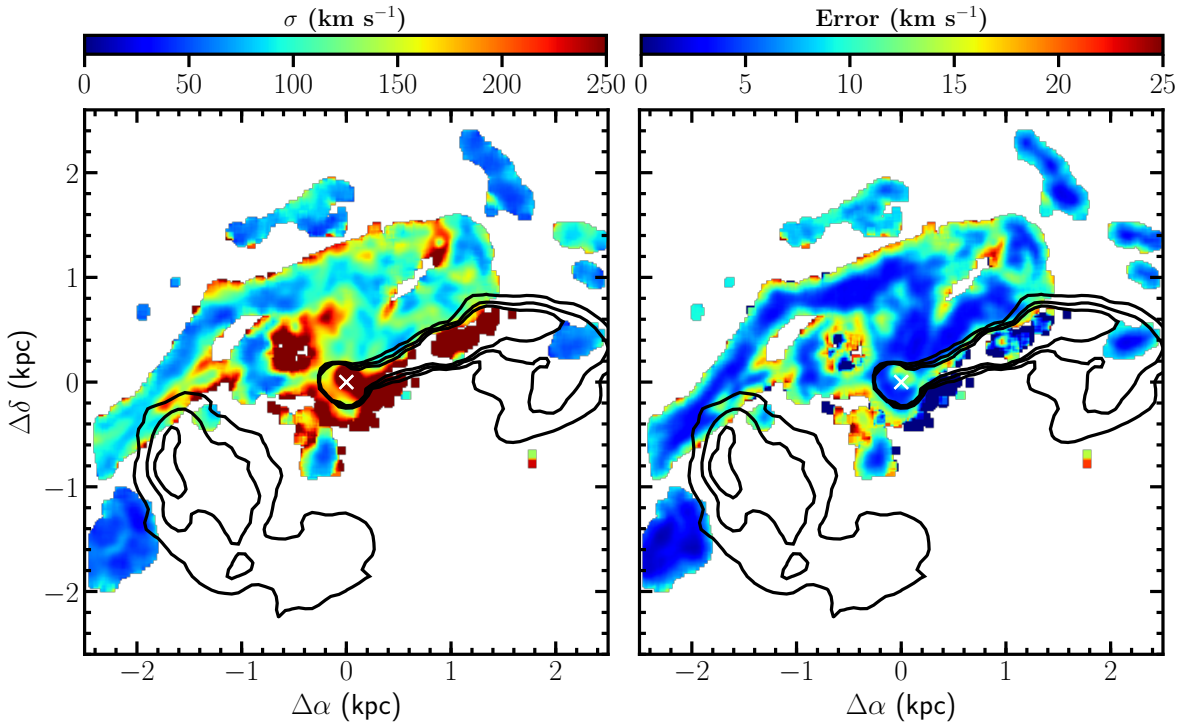

Fig. 6. Velocity dispersion map (*left panel*) and associated error (*right panel*) of the ionised gas derived from MUSE for emission lines with a $S/N > 10$.

the line ratio increases from log([OI]λ6300 Å/Hα) $\simeq -0.7$ to log([OI]λ6300 Å/Hα) $\simeq -0.4$. The dark-blue colour of the points suggests that this tight relation is due to the inner regions close to the AGN. The bulk of the points forms a flatter and much more dispersed relation spanning the whole range in line ratio ($-0.8 \lesssim$ log([OI]λ6300 Å/Hα) $\lesssim 0.3$) but reaching only velocity dispersions up to $\sigma \simeq 300$ km s^{-1}. This trend is due to the main body of the filament (light-blue, cyan, and green points). The regions located at the edge of the counter-jet (red points) do not show any relation. The tight and steep relation in the inner region (dark-blue points) is also clear in the σ versus [NII]λ6584/Hα and [SII]λ6716,6731 Å/Hα line-ratio diagrams. In these two other diagrams, however, the bulk of the points does not follow the σ versus line-ratio relation observed in the [OI] line. In particular,

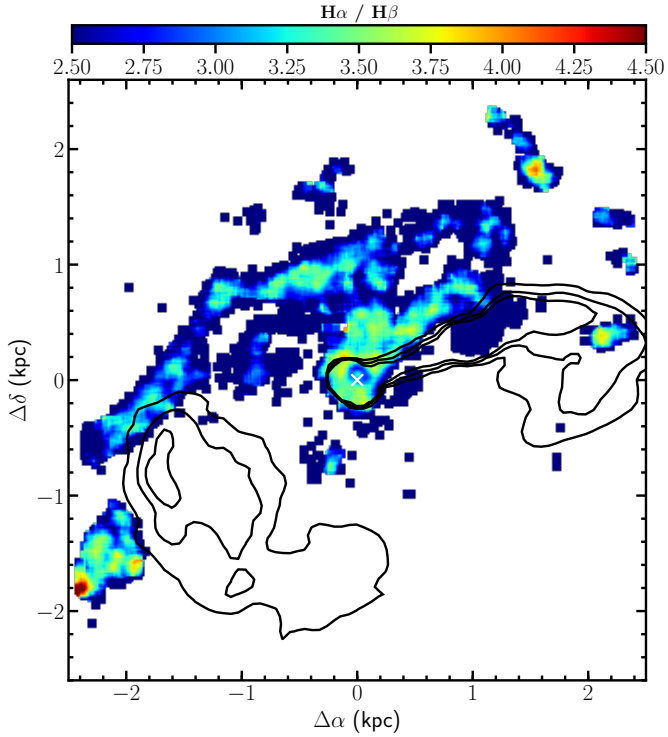

Fig. 7. Distribution of the Balmer decrement derived for emission lines with a $S/N > 5$.

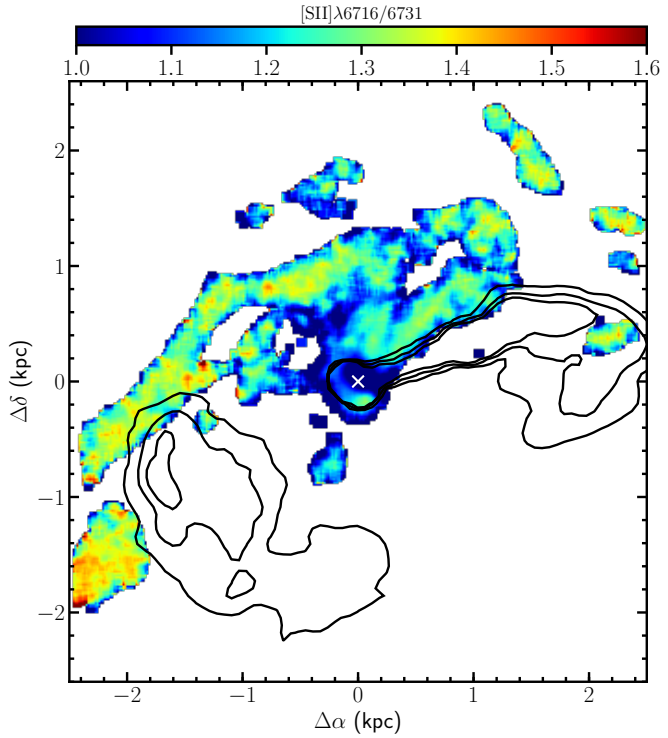

Fig. 8. Distribution of the [SII]λ6716 Å/[SII]λ6731 Å ratio for emission lines with a $S/N > 5$.

we note that those located at the southeast edge of the filament observed by MUSE, at ≃2 kpc from the nucleus of the galaxy (red points), have the lowest velocity dispersions but the highest [NII]λ6584/Hα and [SII]λ6716,6731 Å/Hα line ratios within the MUSE field.

3.3. Comparison with other bands

The spectacular images at hand allow us to make a detailed comparison between the distribution of the ionised gas emission and the other components of the ISM of the galaxy. Figure 12 shows, with a sensitivity and resolution never reached before now (Sparks et al. 1993, 2004; Werner et al. 2013), how the hot gas traced by the X-rays emission from *Chandra* compares with the ionised gas emission. As can be noted from previous works (Sparks et al. 1993, 2004; Werner et al. 2013), at large scale the main ionised gas filaments are not associated with the hot gas distribution which has a structured shape only in the 0.5–1.0 and 1.0–3.5 keV bands, while at smaller scales the coincidence between well defined features is present (e.g. Sparks et al. 2004). We note that the plume of ionised gas first detected by Gavazzi et al. (2000) at ≃15 kpc to the east, and the extended low-surface-brightness filament ≃3 kpc to the east of this plume, at ≃18 kpc from the nucleus, first detected in this work, correspond to sharp edges in the X emission in the 0.5–1.0 and 1.0–3.5 keV bands.

Figure 13 shows the comparison between the ionised gas distribution traced by the Hα+[NII] and the distribution of the dust component as derived by the NGVS image (see Sect. 3.3). As already noticed by Sparks et al. (1993), there is quite a clear association between the northwest filament located just on the northern side of the jet and a dust lane. The extremely deep NGVS image allowed us to detect several other previously unknown dust features. Most of them are clearly also associated with prominent ionised gas filaments, such as for example the structure at ≃14 arcsec (≃1 kpc) to the north of the nucleus called "bar structure" in Sparks et al. (2004), although dust and ionised gas are distributed here in a different way, the former on a circular loop, the latter along an elongated structure. Dust is also present on the "patch" at ≃10 arcsec (≃800 pc) south to the nucleus, and in a bright region at ≃10 arcsec (≃800 pc) to the west. There is also a clear association in the four ionised gas filaments to the northwest, west, and southwest of the nucleus, at roughly 24–32 arcsec (1.9–2.6 kpc). Because the surface brightness of the galaxy rapidly decreases outward, we are not able to detect dust in absorption at distances larger than ≃30–35 arcsec (2.4–2.8 kpc), and we therefore do not know whether the long southeastern filament is associated with any dusty feature.

We can also compare the distribution of the ionised gas to that of the cold gas component derived from the ^{12}CO(2-1) line by Simionescu et al. (2018) using ALMA data and from the [CII] line by Werner et al. (2013). Since the gas has only been detected in a very limited region at the edge of the counter-jet in the southeastern direction, we show the comparison on a zoomed region (Fig. 14). The cold gas, which has a mass of $M(H_2) \simeq 5 \times 10^5\, M_\odot$, is located on a peak of ionised gas emission. We do not see, however, any associated compact source in either the broad- or narrow-band images, indicating a lack of any star forming system.

Figure 15 compares the ionised gas emission to the radio continuum emission at 115 GHz. As already noticed in previous works, the ionised gas emission is located north of the prominent jet, and avoids the counter-jet lobe to the southeast. As a final image, we show in Fig. 16 the pseudo-colour image of M 87 obtained by combining *Chandra* 1.0–3.5 keV, Hα+[NII] and radio continuum at 90 cm frames of the galaxy. This figure allows us to appreciate how the emission at these different wavelengths correlates at large scale. Again we see how the Hα emission avoids the main radio structures in the inner regions (Sparks et al. 1993), while the ionised gas plume and filaments

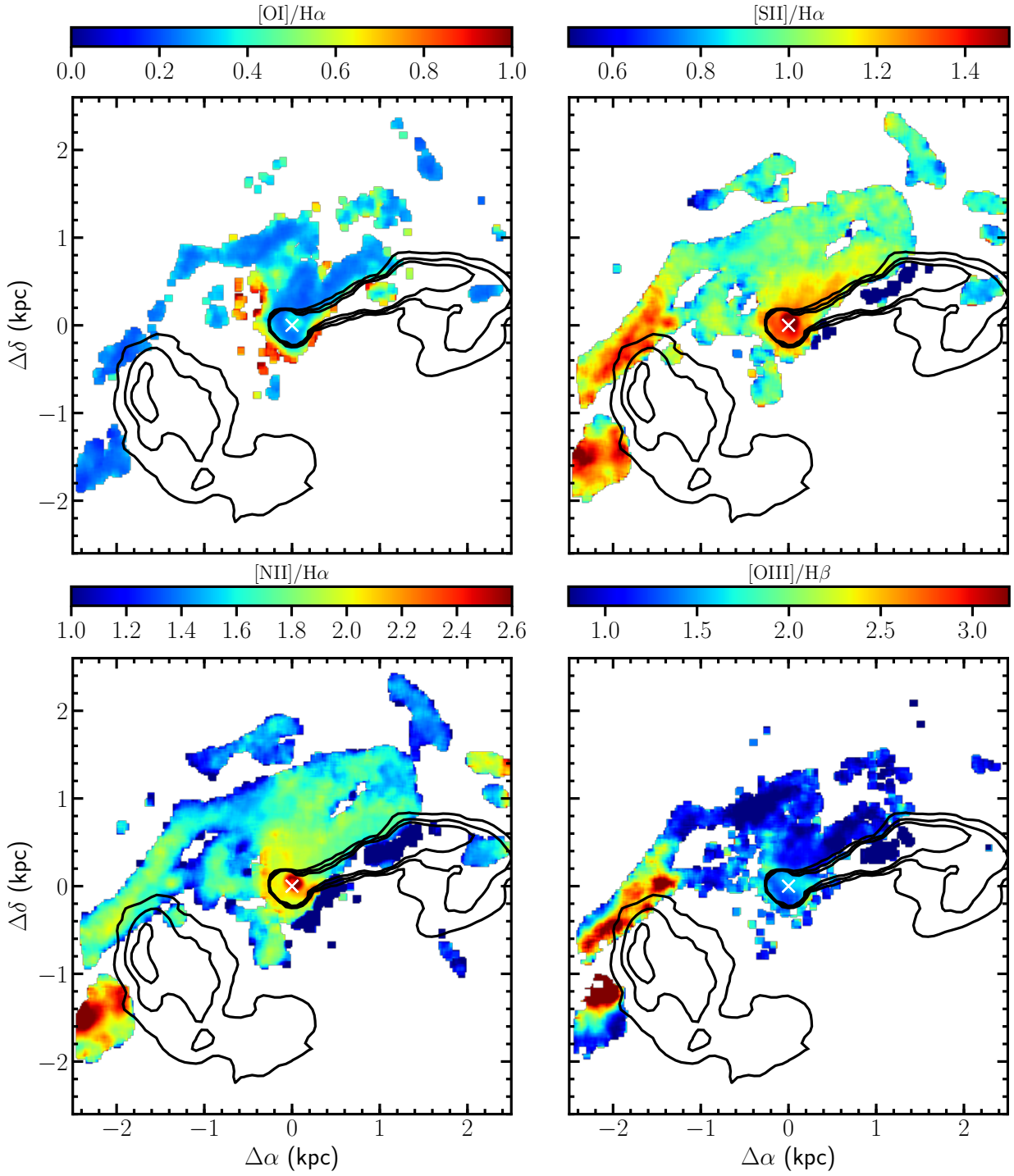

Fig. 9. Distribution of the line ratios [OI]λ6300 Å/Hα (*upper left panel*), [SII]λ6716,6731 Å/Hα (*upper right panel*), [NII]λ6548,6583 Å/Hα (*lower left panel*), and [OIII]λ5007 Å/Hα (*lower right panel*) line ratios for emission lines with a $S/N > 5$.

at ≃15 and 18 kpc east of the nucleus are located within the radio lobe (Gavazzi et al. 2000).

4. Discussion

The properties of the different gas phases of M 87 have been discussed in several publications (e.g. Sparks et al. 1993, 2004; Churazov et al. 2008; Werner et al. 2010, 2013; Simionescu et al. 2018). We therefore refer the reader to these works. Here we focus on the main novel results provided by our data, which are mainly due to their higher sensitivity and angular resolution with respect to those gathered in previous works.

4.1. The source of ionisation

The exquisite quality of the MUSE data allowed us to make a 2D BPT diagram along the ionised gas filament which we compared to the prediction of the photoionisation models of Kewley et al. (2001). Figure 10 (upper panels) clearly shows that in the case of photoionisation the [NII]/Hα line ratio is expected to increase with increasing metallicity, but it never reaches the values observed in the gas filaments of M 87. We recall that in Virgo the metallicity of the ICM derived from ASCA is only 0.39–0.55 $Z_\odot$ (Matsumoto et al. 2000; Fukazawa et al. 2004). Photoionisation due to young massive stars does not seem to be

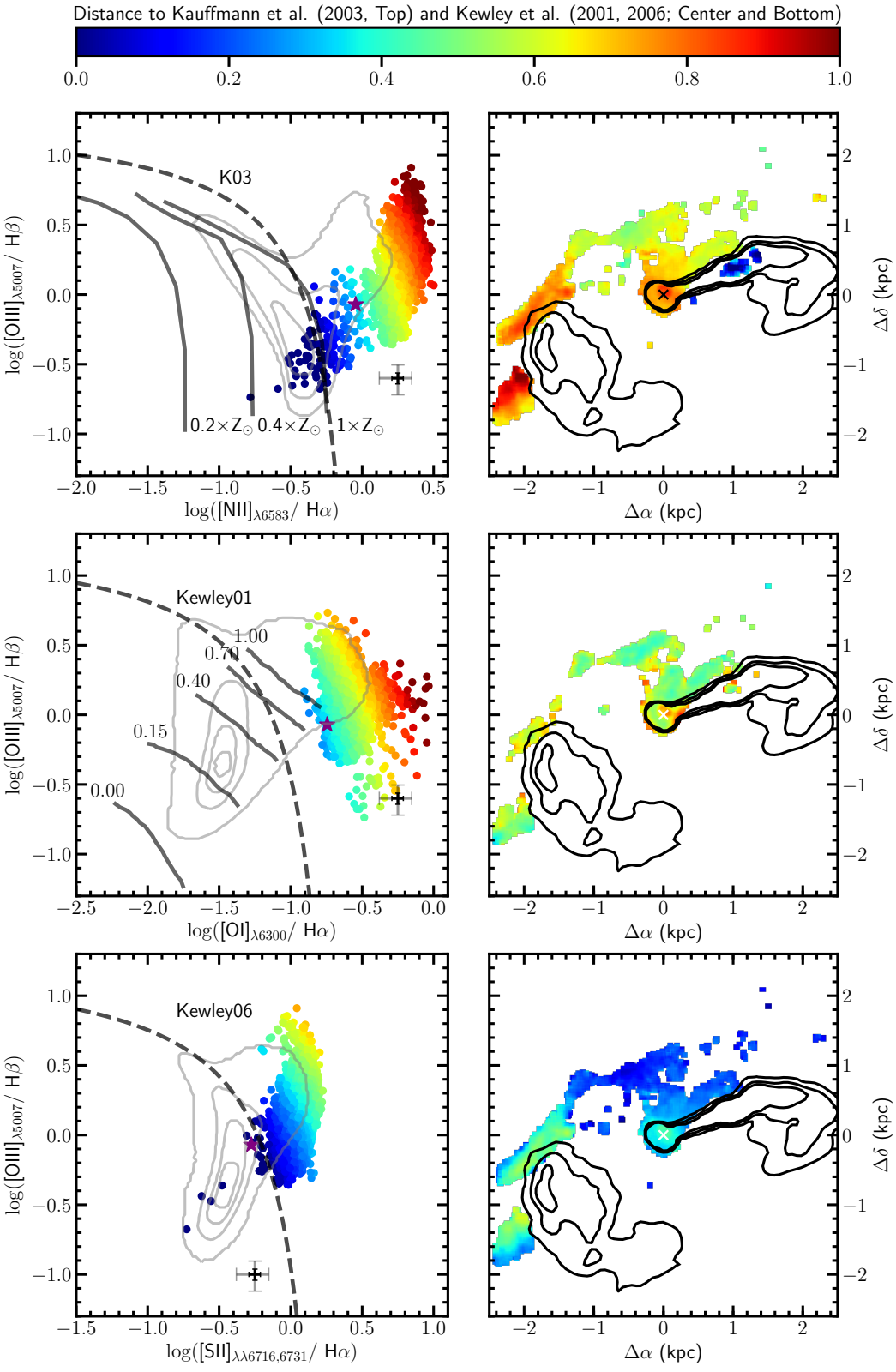

Fig. 10. *Left column*: [OIII]/Hβ vs. [NII]/Hα (*top*), [OIII]/Hβ vs. [OI]/Hα (*centre*), and [OIII]/Hβ vs. [SII]/Hα (*bottom*) BPT diagrams for emission lines with a $S/N > 5$. The dashed curves separate AGN from HII regions (Kauffmann et al. 2003; Kewley et al. 2001, 2006). Data are colour coded according to their minimum distance from these curves. The black and grey crosses indicate the typical error on the data for lines with $S/N \simeq 15$ and $S/N \simeq 5$, respectively. The grey contours show the distribution of a random sample of nuclear spectra of SDSS galaxies in the redshift range 0.01–0.1 and stellar masses $10^9 \leq M_{\rm star} \leq 10^{11}\,M_\odot$. The magenta star shows the position in the diagram of the plume of ionised gas observed at 15 kpc to the east by Gavazzi et al. (2000). The thick solid lines in the *upper left panel* show three different photo-ionisation models at different metallicities (0.2, 0.4, 1 $Z_\odot$; Kewley et al. 2001), those in the *middle left panel* show the shock models of Rich et al. (2011) for increasing shock fractions (from left to right) in a twice-solar gas. *Right column*: map of the spaxel distribution colour-coded according to their position in the BPT diagram.

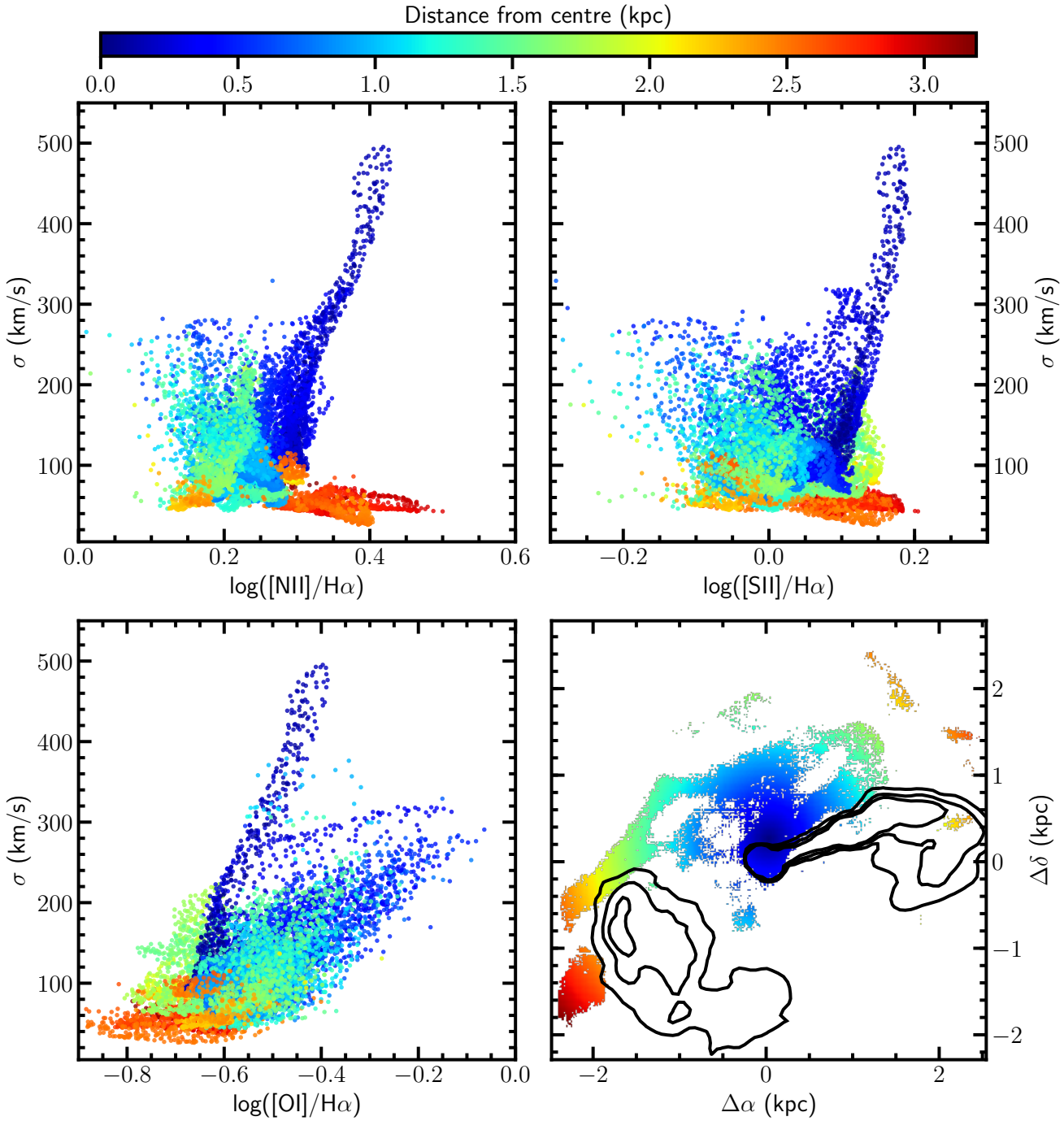

Fig. 11. Relationship between the velocity dispersion in the ionsied gas and the shock-sensitive line ratios [NII]λ6584/Hα (*upper left panel*), [SII]λ6716,6731 Å/Hα (*upper right panel*), and [OI]λ6300 Å/Hα (*lower left panel*) measured for emission lines with a $S/N > 3$ (and $S/N > 10$ for the determination of the velocity dispersion as described in Sect. 2.2). Each point is colour-coded according to its distance from the galaxy centre, as indicated in the *right lower panel*.

at play even in the prominent ionised gas region at the south-eastern edge of the counter-jet, where molecular gas has been detected (Fig. 14). Indeed, we do not observe any compact stellar counterpart in either the UV or optical images, and we therefore deduce that there is no star formation associated with these molecular clouds. We recall that Simionescu et al. (2018), using dynamical arguments, concluded that because of its velocity dispersion of 27 km s^{-1}, the molecular gas within is stable, and is therefore highly unlikely to collapse to form new stars. Positive feedback does not seem to be present in this object. This result is consistent with the findings of Johnstone et al. (2007) after comparing the predictions of photoionisation models with the optical and infrared line properties of cooling-flow galaxies in the core of clusters. Other sources of ionisation have been proposed, such as the pure collisional heating due to cosmic rays accelerated by magnetohydrodynamic waves present along the filament (Ferland et al. 2009; McDonald et al. 2012), dust scattering (Mattila et al. 2007; Seon & Witt 2012), thermal conduction from the hot phase (Sparks et al. 2004), or ionisation due to the central AGN. The deep optical image shown in Fig. 3 indicates that dust is not ubiquitously distributed along the filament, contrary to what is found in other bright central galaxies (e.g. NGC 4696,

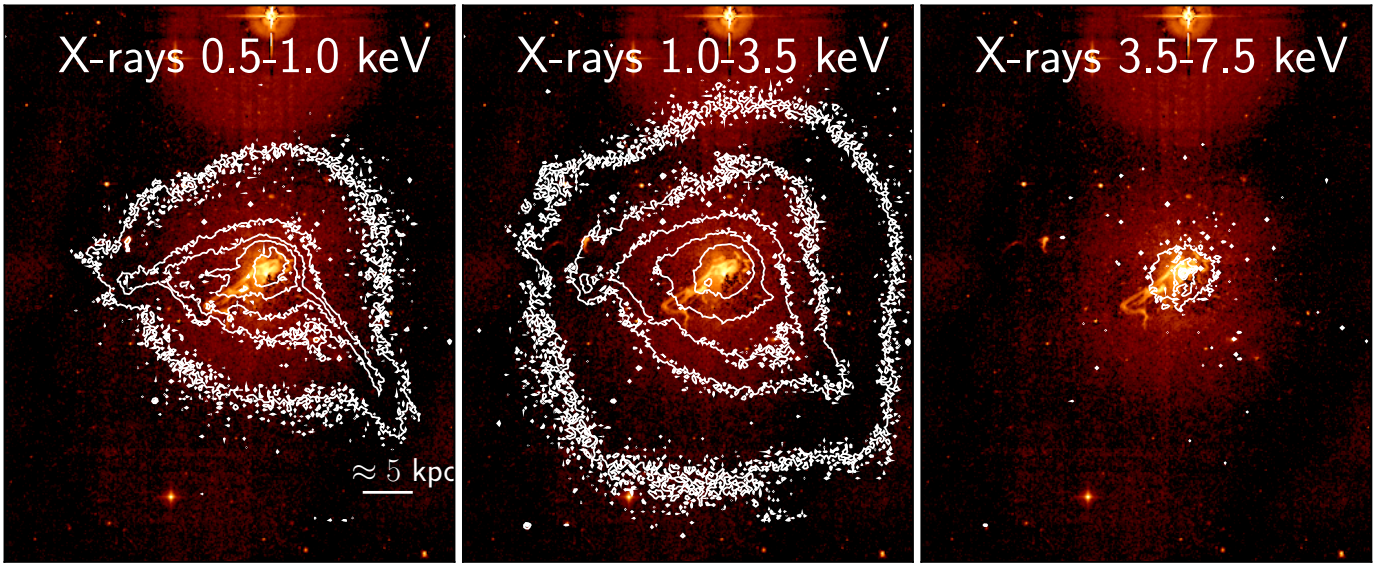

Fig. 12. Comparison between the Hα+[NII] emission (in colour) and the X-rays emission (contours) in the three bands 0.5–1.0 keV (*left panel*), 1.0–3.5 keV (*centre panel*), and 3.5–7.0 keV (*right panel*) in white contours (from Forman et al. 2007).

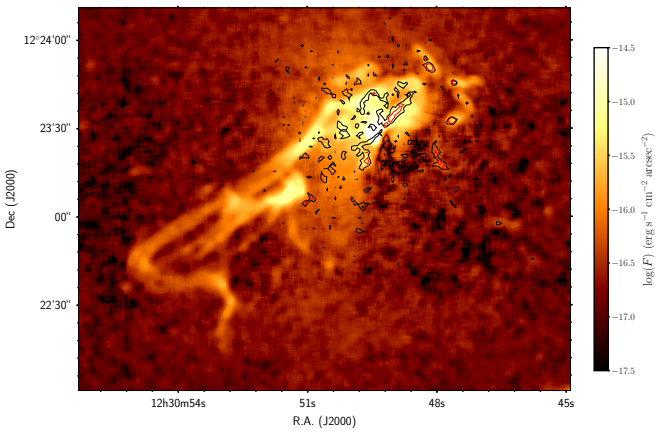

Fig. 13. Comparison between the Hα+[NII] emission (in colour) and the dust distribution (contours) derived from the NGVS image in absorption.

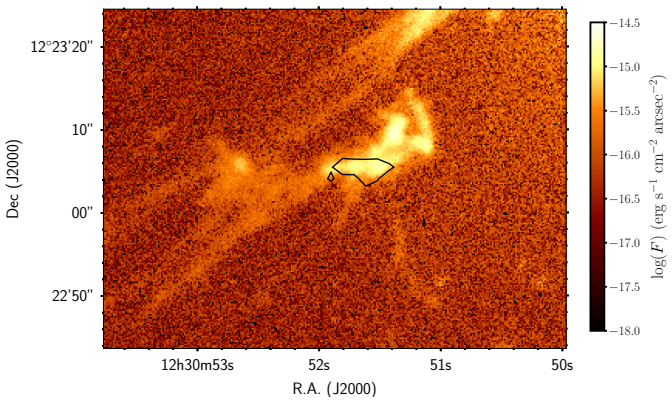

Fig. 14. ALMA ^{12}CO(2-1) line emission contour at 2 mJy beam^{-1} overplotted on the Hα+[NII] image. The molecular gas was detected at ~40″ southeast from the nucleus of M 87. The Hα filament is located at the southeast edge of the cavity formed by the counter-jet.

Crawford et al. 2005). Ionisation from the AGN might be important in the central 0.5 kpc region as suggested by the radial gradient of the [NII]/Hα line ratio with radius and the relatively high [OIII]/Hα ratio (Fig. 10), while it is probably negligible in the outer filament (McDonald et al. 2012). Our analysis also suggests that the gas might be ionised by shocks (Fig. 11). The distribution of the ionised gas at the edges of the radio jet or of the counter-jet might indicate that the shocks can be produced by the energy injected by the AGN in the ISM. The contribution of shocks to the ionisation of the prominent gas filaments of M 87 seems more important than in other central galaxies in cooling flow clusters given its higher [OIII]/Hα line ratio (McDonald et al. 2012).

4.2. The origin of the filament

The kinematical properties of the gas (Fig. 5) compared with those recently derived from the planetary nebulae (Longobardi et al. 2015, 2018) and the globular clusters (Romanowsky et al. 2012) in the outer halo, from the stellar kinematics in the inner regions (Emsellem et al. 2014; Arnold et al. 2014), or from the observed substructures in the colour distribution of the globular clusters (Powalka et al. 2018), seem to suggest that the ionised gas filament is the remnant of a gas-rich galaxy which has recently been accreted by M 87, as first proposed by Sparks et al. (1993), or has crossed the halo losing most of its gas reservoir after a ram-pressure-stripping event (Mayer et al. 2006). The rough estimate of the total mass of the ionised gas in the filament ($M_{\rm filament} \simeq 6.9 \times 10^7\ M_\odot$) is comparable to that of the gas that would have been associated with the observed dusty filaments if this dust had been accreted from an external object ($M_{\rm gas,dust} \simeq 2 \times 10^7\ M_\odot$). This gas mass, however, should be considered as a lower limit to the total gas mass lost by the star-forming galaxy because dust might have been destroyed by sputtering in the harsh intertsellar radiation field of M 87 (Goudfrooij & de Jong 1995; Temi et al. 2007). The kinematical properties of approximately 300 planetary nebulae in the outer halo and a detailed colour analysis of the galaxy led Longobardi et al. (2015, 2018) to conclude that M 87 has recently ($\lesssim$1 Gyr) accreted a massive ($M_{\rm star} \simeq 6{\times}10^9\ M_\odot$) star forming system. The comparison between the distribution of about 500 globular clusters in the phase diagram with tuned simulations suggests that the galaxy has been continuously accreting smaller systems for ~1 Gyr (Romanowsky et al. 2012).

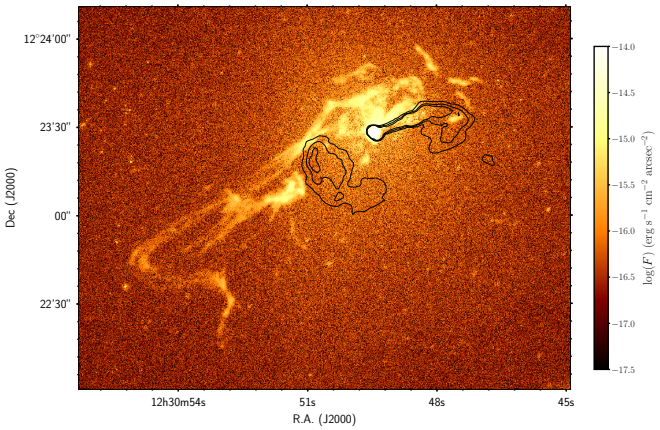

Fig. 15. ALMA contours in the radio continuum at 115 GHz of M 87 at levels of 1.5, 5, 10 mJy beam^{-1} overplotted on the continuum-subtracted Hα+[NII] image.

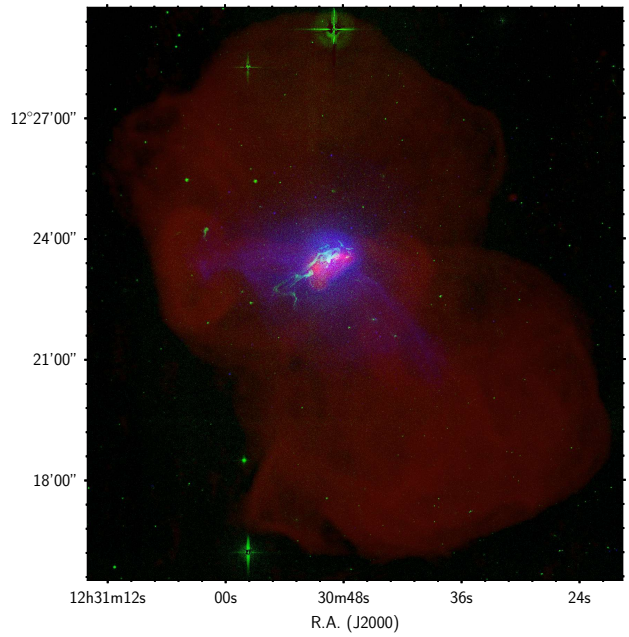

Fig. 16. Pseudo-colour image of M 87 obtained by combining *Chandra* 1.0–3.5 keV (blue), VESTIGE Hα+[NII] (green), and the VLA radio continuum at 90 cm (red) frames of the galaxy.

Furthermore, M 87 has also a kinematically distinct component in the inner ∼1.2 kpc-radius which might have been formed after a gravitational perturbation (Emsellem et al. 2014). Accretion of satellites is also suggested by the low-surface-brightness fine structures in the deep optical image of M 87 (Mihos et al. 2017). The complex kinematics along the filament rules out a simple scenario where the gas has been lost while the star forming progenitor was spiraling around M 87, as observed in the central galaxy of the cluster A2052 (Balmaverde et al. 2018), becoming virialised on short timescales as expected in massive objects. Indeed, the energy ejected by the AGN can mix, excite, and accelerate the gas which is conserving its angular momentum while infalling within the potential well of the galaxy, producing the peculiar velocity field shown in Fig. 5. Complex structures in the velocity field of the ionised gas filaments have been observed in other radio galaxies such as NGC 1275 in Perseus (Gendron-Marsolais et al. 2018), where star formation is also present (Canning et al. 2014).

An alternative interpretation is that, as in other central cluster galaxies, the ionised gas filament might be produced by the diffuse hot gas halo which, for local instabilities, cools out to form magnetically supported narrow filaments. The velocity map shown in Fig. 5 reveals generally negative velocities for the gas adjacent to the jet and positive velocities on the other side. This is in general consistent with the scenario that at least some ionised emitting gas interacts with jets and the counter-jet. Indeed, the ionised gas filaments of M 87 avoids the radio bubbles (Figs. 15 and 16) as often observed in cooling-flow galaxies (Russell et al. 2017). Jets can trigger buoyant bubbles filled by radio plasma, rising in the X-ray atmosphere of M 87 (Churazov et al. 2001). This kind of rising bubble can have velocities of 60–70% of the local sound speed, or 300–470 km s^{-1} for kT = 1−1.8 keV (Million et al. 2010). The ionised gas filaments to the south-east align with the current jet/counter jet, and might have been formed out of thermal instabilities in uplift gas from the central region by radio bubbles (e.g. Churazov et al. 2001; Forman et al. 2007). The ionised gas inside the radio contours in the western direction might therefore be at the edges of the radio bubble (projection effects).

5. Conclusions

The analysis of deep narrow-band Hα+[NII] images of the elliptical radio galaxy M 87 in the centre of the Virgo cluster confirmed the presence of an ionised gas filament extending up to 3 kpc to the northwest and 8 kpc to the southeast. It also allowed the detection of a low-surface-brightness plume of ionised gas at ≃18 kpc to the east of the nucleus, located at the edge of the radio continuum counter-jet lobe and corresponding to a sharpe edge in the 0.5–1.0 keV X-ray emission. The kinematical properties of this gas filament derived using new MUSE IFU data revealed the presence of a very perturbed velocity field, with differences in velocity as high as ∼800 km s^{-1} on scales ≲1 kpc, probably due to different gas components located along the line of sight. The position of the spaxels along several diagnostic diagrams, and the observed relationship between the shock-sensitive [OI]/Hα line ratio and the velocity dispersion of the gas, consistently suggest that the gas is shock-ionised probably by the expanding bubbles of the rotating radio jet. The mass of the ionised gas in the filament, or that of the cold gas expected to be associated with the dust seen in absorption (both a few 10^7 $M_\odot$) might suggest that the filament is a remnant of gas coming from a galaxy recently captured by M 87. The ionised gas filament, however, could also be gas cooled out from the hot gas halo along magnetically supported narrow filaments.

Acknowledgements. We thank the anonymous referee for constructive comments. We thank N. Grosso for his help in gathering the *Chandra* X-ray data of M 87. We are grateful to the whole CFHT team who assisted us in the preparation and in the execution of the observations and in the calibration and data reduction: Todd Burdullis, Daniel Devost, Bill Mahoney, Nadine Manset, Andreea Petric, Simon Prunet, Kanoa Withington. We acknowledge financial support from "Programme National de Cosmologie and Galaxies" (PNCG) funded by CNRS/INSU-IN2P3-INP, CEA and CNES, France, and from "Projet International de Coopération Scientifique" (PICS) with Canada funded by the CNRS, France. This research has made use of the NASA/IPAC Extragalactic Database (NED) which is operated by the Jet Propulsion Laboratory, California Institute of Technology, under contract with the National Aeronautics and Space Administration and of the GOLDMine database (http://goldmine.mib.infn.it/) (Gavazzi et al. 2003). This project has received funding from the European Research Council (ERC) under the European Union's Horizon 2020 research and innovation programme (grant agreement No. 757535 and grant agreement No. 679627, project name FORNAX). MB acknowledges the FONDECYT regular grant 1170618. MS acknowledges support from the NSF grant 1714764.

References

Anderson, M. E., & Sunayaev, R. 2018, A&A, 617, A123
Arnold, J. A., Romanowsky, A. J., Brodie, J. P., et al. 2014, ApJ, 791, 80
Arp, H. C. 1967, Astrophys. Lett., 1, 1
Baade, W., & Minkowski, R. 1954, ApJ, 119, 206
Baes, M., Clemens, M., Xilouris, E. M., et al. 2010, A&A, 518, L53
Baldwin, J. A., Phillips, M. M., & Terlevich, R. 1981, PASP, 93, 5
Balmaverde, B., Capetti, A., Marconi, A., & Venturi, G. 2018, A&A, 612, A19
Baum, S. A., Heckman, T. M., Bridle, A., van Breugel, W. J. M., & Miley, G. K. 1988, ApJS, 68, 643
Belfiore, F., Maiolino, R., Maraston, C., et al. 2016, MNRAS, 461, 3111
Bellhouse, C., Jaffé, Y. L., Hau, G. K. T., et al. 2017, ApJ, 844, 49
Bellini, A., Renzini, A., Anderson, J., et al. 2015, ApJ, 805, 178
Bendo, G. J., Galliano, F., & Madden, S. C. 2012, MNRAS, 423, 197
Boroson, T. A., Thompson, I. B., & Shectman, S. A. 1983, AJ, 88, 1707
Boselli, A., Cortese, L., Deharveng, J. M., et al. 2005, ApJ, 629, L29
Boselli, A., Boissier, S., Cortese, L., et al. 2009, ApJ, 706, 1527
Boselli, A., Ciesla, L., Buat, V., et al. 2010, A&A, 518, L61
Boselli, A., Boissier, S., Heinis, S., et al. 2011, A&A, 528, A107
Boselli, A., Voyer, E., & Boissier, S. 2014, A&A, 570, A69
Boselli, A., Cuillandre, J. C., Fossati, M., et al. 2016, A&A, 587, A68
Boselli, A., Fossati, M., Ferrarese, L., et al. 2018a, A&A, 614, A56
Boselli, A., Fossati, M., Cuillandre, J. C., et al. 2018b, A&A, 615, A114
Byrd, G., & Valtonen, M. 1990, ApJ, 350, 89
Canning, R. E. A., Ryon, J. E., Gallagher, J. S., et al. 2014, MNRAS, 444, 336
Cappellari, M., & Emsellem, E. 2004, PASP, 116, 138
Churazov, E., Brüggen, M., Kaiser, C. R., Böhringer, H., & Forman, W. 2001, ApJ, 554, 261
Churazov, E., Forman, W., Vikhlinin, A., et al. 2008, MNRAS, 388, 1062
Ciambur, B. C. 2015, ApJ, 810, 120
Ciesla, L., Boselli, A., Smith, M. W. L., et al. 2012, A&A, 543, A161
Ciesla, L., Boquien, M., Boselli, A., et al. 2014, A&A, 565, A128
Conselice, C. J., Gallagher, III., J. S., & Wyse, R. F. G. 2001, AJ, 122, 2281
Consolandi, G., Gavazzi, G., Fossati, M., et al. 2017, A&A, 606, A83
Cortese, L., Boissier, S., Boselli, A., et al. 2012, A&A, 544, A101
Cortese, L., Fritz, J., Bianchi, S., et al. 2014, MNRAS, 440, 942
Côté, P., Blakeslee, J. P., Ferrarese, L., et al. 2004, ApJS, 153, 223
Cowie, L. L., & Binney, J. 1977, ApJ, 215, 723
Crawford, C. S., Allen, S. W., Ebeling, H., Edge, A. C., & Fabian, A. C. 1999, MNRAS, 306, 857
Crawford, C. S., Hatch, N. A., Fabian, A. C., & Sanders, J. S. 2005, MNRAS, 363, 216
De Lucia, G., & Blaizot, J. 2007, MNRAS, 375, 2
Dopita, M. A., & Sutherland, R. S. 1995, ApJ, 455, 468
Dopita, M. A., Koratkar, A. P., Allen, M. G., et al. 1997, ApJ, 490, 202
Dwarakanath, K. S., van Gorkom, J. H., & Owen, F. N. 1994, ApJ, 432, 469
Emsellem, E., Krajnović, D., & Sarzi, M. 2014, MNRAS, 445, L79
Fabian, A. C. 1994, ARA&A, 32, 277
Fabian, A. C., & Nulsen, P. E. J. 1977, MNRAS, 180, 479
Ferland, G. J., Fabian, A. C., Hatch, N. A., et al. 2009, MNRAS, 392, 1475
Ferrarese, L., Côté, P., Jordán, A., et al. 2006, ApJS, 164, 334
Ferrarese, L., Côté, P., Cuillandre, J.-C., et al. 2012, ApJS, 200, 4
Fitzpatrick, E. L. 1999, PASP, 111, 63
Ford, H. C., & Butcher, H. 1979, ApJS, 41, 147
Forman, W., Jones, C., Churazov, E., et al. 2007, ApJ, 665, 1057
Forman, W., Churazov, E., Jones, C., et al. 2017, ApJ, 844, 122
Fossati, M., Fumagalli, M., Boselli, A., et al. 2016, MNRAS, 455, 2028
Fossati, M., Mendel, J. T., Boselli, A., et al. 2018, A&A, 614, A57
Franx, M., & Illingworth, G. 1990, ApJ, 359, L41
Fukazawa, Y., Makishima, K., & Ohashi, T. 2004, PASJ, 56, 965
Fumagalli, M., Fossati, M., Hau, G. K. T., et al. 2014, MNRAS, 445, 4335
Gavazzi, G., Boselli, A., Scodeggio, M., Pierini, D., & Belsole, E. 1999, MNRAS, 304, 595
Gavazzi, G., Boselli, A., Vílchez, J. M., Iglesias-Paramo, J., & Bonfanti, C. 2000, A&A, 361, 1
Gavazzi, G., Boselli, A., Donati, A., Franzetti, P., & Scodeggio, M. 2003, A&A, 400, 451
Gavazzi, G., Consolandi, G., Pedraglio, S., et al. 2018, A&A, 611, A28
Gendron-Marsolais, M., Hlavacek-Larrondo, J., Martin, T. B., et al. 2018, MNRAS, 479, L28
Gomes, J. M., Papaderos, P., Kehrig, C., et al. 2016, A&A, 588, A68
Goudfrooij, P., & de Jong, T. 1995, A&A, 298, 784
Gwyn, S. D. J. 2008, PASP, 120, 212
Heckman, T. M., Baum, S. A., van Breugel, W. J. M., & McCarthy, P. 1989, ApJ, 338, 48
Hines, D. C., Eilek, J. A., & Owen, F. N. 1989, ApJ, 347, 713
Ho, I.-T., Kewley, L. J., Dopita, M. A., et al. 2014, MNRAS, 444, 3894
Johnstone, R. M., Hatch, N. A., Ferland, G. J., et al. 2007, MNRAS, 382, 1246
Kauffmann, G., Heckman, T. M., Tremonti, C., et al. 2003, MNRAS, 346, 1055
Kaviraj, S., Schawinski, K., Devriendt, J. E. G., et al. 2007, ApJS, 173, 619
Kennicutt, Jr., R. C. 1998, ARA&A, 36, 189
Kewley, L. J., Dopita, M. A., Sutherland, R. S., Heisler, C. A., & Trevena, J. 2001, ApJ, 556, 121
Kewley, L. J., Groves, B., Kauffmann, G., & Heckman, T. 2006, MNRAS, 372, 961
Longobardi, A., Arnaboldi, M., Gerhard, O., & Mihos, J. C. 2015, A&A, 579, L3
Longobardi, A., Arnaboldi, M., Gerhard, O., Pulsoni, C., & Soldner-Rembold, I. 2018, A&A, 620, A111
Malumuth, E. M., & Richstone, D. O. 1984, ApJ, 276, 413
Matsumoto, H., Tsuru, T. G., Fukazawa, Y., Hattori, M., & Davis, D. S. 2000, PASJ, 52, 153
Mattila, K., Juvela, M., & Lehtinen, K. 2007, ApJ, 654, L131
Mayer, L., Mastropietro, C., Wadsley, J., Stadel, J., & Moore, B. 2006, MNRAS, 369, 1021
McDonald, M., Veilleux, S., Rupke, D. S. N., & Mushotzky, R. 2010, ApJ, 721, 1262
McDonald, M., Veilleux, S., & Rupke, D. S. N. 2012, ApJ, 746, 153
Mei, S., Blakeslee, J. P., Côté, P., et al. 2007, ApJ, 655, 144
Merritt, D. 1985, ApJ, 289, 18
Mihos, J. C., Harding, P., Feldmeier, J. J., et al. 2017, ApJ, 834, 16
Million, E. T., Werner, N., Simionescu, A., et al. 2010, MNRAS, 407, 2046
O'Connell, R. W. 1999, ARA&A, 37, 603
Osterbrock, D. E., & Ferland, G. J. 2006, Astrophysics of Gaseous Nebulae and Active Galactic Nuclei, 2nd. edn. (Sausalito, CA: University Science Books)
Ostriker, J. P., & Tremaine, S. D. 1975, ApJ, 202, L113
Owen, F. N., Eilek, J. A., & Kassim, N. E. 2000, ApJ, 543, 611
Perlman, E. S., Mason, R. E., Packham, C., et al. 2007, ApJ, 663, 808
Poggianti, B. M., Moretti, A., Gullieuszik, M., et al. 2017, ApJ, 844, 48
Powalka, M., Puzia, T. H., Lançon, A., et al. 2018, ApJ, 856, 84
Proxauf, B., Öttl, S., & Kimeswenger, S. 2014, A&A, 561, A10
Rich, J. A., Kewley, L. J., & Dopita, M. A. 2011, ApJ, 734, 87
Rich, J. A., Kewley, L. J., & Dopita, M. A. 2015, ApJS, 221, 28
Roediger, J. C., Courteau, S., McDonald, M., & MacArthur, L. A. 2011, MNRAS, 416, 1983
Romanowsky, A. J., Strader, J., Brodie, J. P., et al. 2012, ApJ, 748, 29
Russell, H. R., McNamara, B. R., Fabian, A. C., et al. 2017, MNRAS, 472, 4024
Sabra, B. M., Shields, J. C., Ho, L. C., Barth, A. J., & Filippenko, A. V. 2003, ApJ, 584, 164
Sarazin, C. L. 1986, Rev. Mod. Phys., 58, 1
Sarzi, M., Falcón-Barroso, J., Davies, R. L., et al. 2006, MNRAS, 366, 1151
Sarzi, M., Spiniello, C., La Barbera, F., Krajnović, D., & van den Bosch, R. 2018, MNRAS, 478, 4084
Schlafly, E. F., & Finkbeiner, D. P. 2011, ApJ, 737, 103
Schlegel, D. J., Finkbeiner, D. P., & Davis, M. 1998, ApJ, 500, 525
Seon, K.-I., & Witt, A. N. 2012, ApJ, 758, 109
Simionescu, A., Tremblay, G., Werner, N., et al. 2018, MNRAS, 475, 3004
Sparks, W. B., Ford, H. C., & Kinney, A. L. 1993, ApJ, 413, 531
Sparks, W. B., Donahue, M., Jordán, A., Ferrarese, L., & Côté, P. 2004, ApJ, 607, 294
Sparks, W. B., Pringle, J. E., Donahue, M., et al. 2009, ApJ, 704, L20
Sparks, W. B., Pringle, J. E., Carswell, R. F., et al. 2012, ApJ, 750, L5
Spector, O., Finkelman, I., & Brosch, N. 2012, MNRAS, 419, 2156
Suh, H., Jeong, H., Oh, K., et al. 2010, ApJS, 187, 374
Temi, P., Brighenti, F., & Mathews, W. G. 2007, ApJ, 660, 1215
van Gorkom, J. H., Knapp, G. R., Ekers, R. D., et al. 1989, AJ, 97, 708
Vazdekis, A., Sánchez-Blázquez, P., Falcón-Barroso, J., et al. 2010, MNRAS, 404, 1639
Young, A. J., Wilson, A. S., & Mundell, C. G. 2002, ApJ, 579, 560
Weil, M. L., Bland-Hawthorn, J., & Malin, D. F. 1997, ApJ, 490, 664
Werner, N., Simionescu, A., Million, E. T., et al. 2010, MNRAS, 407, 2063
Werner, N., Oonk, J. B. R., Canning, R. E. A., et al. 2013, ApJ, 767, 153
White, S. D. M. 1976, MNRAS, 174, 19